GEOPHYSICAL RESEARCH LETTERS, VOL. ???, XXXX, DOI:10.1029/,

Correlations between enhanced electron temperatures and electric field wave power in the Martian ionosphere

C.M. Fowler,[1] L. Andersson,[1] W.K. Peterson,[1] J. Halekas,[2] A.F. Nagy,[3] R.E. Ergun,[1] J. Espley,[4] D.L. Mitchell,[5] J.E.P. Connerney,[4] C. Mazelle,[6,7] P.R. Mahaffy,[4] B.M. Jakosky[1]

1. Key points

1. Correlations exist between observed electron temperature and total electric field wave power in Mars' ionosphere.

2. Electron temperature can be enhanced by over 1000 K for the largest observed wave powers.

3. The observed heating can account for a large fraction of reported discrepancies between modeled and observed electron temperatures.

Corresponding author: C. M. Fowler, Laboratory of Atmospheric and Space Sciences, University of Colorado, Boulder, Colorado, 80303, USA. (christopher.fowler@lasp.colorado.edu)

[1]Laboratory of Atmospheric and Space

Statistical correlations are reported between measured electron temperatures and total electric field wave power (in the 2-100 Hz frequency range), at Mars' sub-solar point ionosphere. The observations, made by the MAVEN spacecraft, suggest that electric field wave power from the Mars-solar wind

Sciences, University of Colorado, Boulder, Colorado, USA.

[2]Department of Physics And Astronomy, University Of Iowa, Iowa City, IA 52242, USA

[3]Department of Atmospheric, Oceanic and Space Sciences, University of Michigan, Ann Arbor, Michigan, USA

[4]NASA Goddard Space Flight Center, Greenbelt, MD 20771, USA

[5]Space Sciences Laboratory, University of California, Berkeley, California, USA.

[6]CNRS, Institut de Recherche en Astrophysique et Planétologie, Toulouse, France

[7]University Paul Sabatier, Toulouse, France

interaction propagates through the Martian ionosphere and is able to heat ionospheric electrons by over 1000 K. Such heating can account for a substantial (but likely not complete) fraction of previously reported discrepancies between modeled and observed electron temperatures in Mars' upper ionosphere. Wave power is typically less than observable thresholds below altitudes of about 200 km, suggesting that energy is deposited into the ionosphere above this. Observed total wave powers range between 10^{-12} and 10^{-9} $(V/m)^2$, and decrease with increasing integrated electron density (or, decreasing altitude).

1. Introduction

The significant differences between measured and modeled plasma temperatures at Venus and Mars has been a topic of investigation for several decades [*Schunk and Nagy*, 2009]. Some of the suggested mechanisms to account for these differences have included topside heat inflow [*Cravens et al.*, 1980; *Choi et al.*, 1998], reduced thermal conductivity [*Cravens et al.*, 1980], and plasma wave heating [*Scarf et al.*, 1980; *Shapiro et al.*, 1995; *Ergun et al.*, 2006]. Using reasonable parameters all of these suggestions have resulted in model values close to the measured values. However, until now, there have been no relevant data to check such suggestions and so this problem has remained unsolved. The Mars Atmosphere and Volatile EvolutioN (MAVEN) mission is providing an opportunity to investigate this problem quantitatively.

The electron temperature, Te, is an important parameter in the investigation of planetary atmospheres. Below the exobase, in the collision dominated photochemical regime, photochemical reaction rates that determine the structure and composition of the atmosphere and ionosphere can be strongly dependent on Te (e.g. Table 2 in *Fox and Dalgarno* [1979], Table 8.5 in *Schunk and Nagy* [2009] and Table 1 in *Andersson et al.* [2010]). The Martian exobase lies between approximately 180 and 220 km, depending upon atmospheric species and local neutral atmospheric conditions (e.g. *Fox* [1993a]). Well below the exobase, collisions between electrons and the much more abundant neutral atmosphere result in the thermalization of Te to the neutral atmospheric temperature.

At altitudes close to and spanning the exobase, Te can significantly impact the escape to space of both hot atomic oxygen (via the dissociative recombination (DR) of $O2^{+}$), and planetary ions (via the electron pressure gradient and subsequent ambi-polar electric field). The exothermic nature of the DR of $O2^+$ (the rate of which is inversely proportional to Te) can produce hot O atoms that possess enough energy to escape the gravitational potential of the planet at their point of production (e.g. *Fox and Hać* [2009]; *Lee et al.* [2015]; *Lillis et al.* [2015]). The longer mean free paths associated with the less collisional nature of the atmosphere around the exobase, mean that a significant fraction of these hot O atoms can escape the planet instead of thermalizing with the neutral atmosphere. At altitudes far above the exobase where collisions occur infrequently, plasma processes dominate at Mars that can strongly influence the ion and electron temperatures and densities. Te is observed to reach $\sim$ 3000 K or greater by about 300 km on the dayside of Mars [*Ergun et al.*, 2015]. The observed gradient in Te is an indication of downward heat flow that brings thermal energy from higher altitudes, thus influencing the electron energy balance. This temperature gradient is also responsible in producing the ambi-polar electric field, that acts to accelerate ions upwards and, if strong enough, possibly out of the ionosphere into space [*Collinson et al.*, 2015; *Ergun et al.*, 2016].

The first in-situ measurements of Te at Mars were made by the Viking landers in 1976 and two altitude profiles were obtained [*Hanson and Mantas*, 1988]. The only other in-situ measurements have been made by the MAVEN spacecraft, and thus, the observationally based nature of this study was not possible prior to MAVEN. Observed Te profiles from Viking and MAVEN are significantly warmer than model predictions above $\sim$ 250 km, typically by 1000-2000 K. One dimensional coupled electron and ion energy equations have been used to model Te; topside heat fluxes or reduced thermal conductivities were required to match the Viking temperature profiles [*Chen et al.*, 1978; *Choi et al.*, 1998]. *Matta et al.* [2014] self consistently solved Te and individual species Ti (ion temperature) under vertical magnetic field conditions across a range of local times. Solar EUV heating alone could not reproduce the Viking profiles and topside heat fluxes were required to obtain agreement above $\sim$ 200 km altitude. *Cui et al.* [2015] investigated a revised Chapman model of the ionospheric peak for altitudes below 200 km. Their results were indicative of topside heat fluxes being present, particularly at the terminators, which were postulated to arise from the Mars-solar wind interaction. *Sakai et al.* [2016] used a two stream suprathermal electron transport code coupled with the energy equation to self consistently solve Te. Their results were able to reproduce the MAVEN LPW temperature profiles by invoking horizontal magnetic fields to thermally isolate the upper ionosphere. Although likely applicable to specific times, this result is unlikely to explain all instances of elevated Te - the Martian ionosphere (including magnetic topology) is highly variable and elevated Te occur too frequently for a specific geometry to explain all instances.

The lack of a global magnetic field at Mars results in a planet-solar wind interaction that occurs much closer to the planet than at magnetized bodies such as the Earth. The small sub-solar shock stand off distance, combined with the relatively large plasma scale lengths at Mars, likely prevents the shocked solar wind from completely thermalizing before encountering the magnetosphere and upper atmosphere of the planet. Thus, particles and waves driven by the solar wind interaction are expected to influence these regions, and are thought to provide some (unknown) fraction of the anomalous heating source that produces the higher than predicted Te [*Moses et al.*, 1988; *Ergun et al.*, 2006;

Fowler et al., 2017]. Indeed, oscillations in magnetic field have been observed down to periapsis altitudes, about 100 km and 130 km, by the Mars Global Surveyor (MGS) and MAVEN spacecraft, respectively (e.g. *Brain et al.* [2002]; *Espley et al.* [2004]; *DiBraccio et al.* [2015]). The ability of MAVEN to measure the (1D) electric and (3D) magnetic field power spectra, and Te, allow for the first time a data based quantitative analysis of plasma heating within the Martian ionosphere to be made. This study presents statistical observations showing that enhancements in electric field wave power correlate to warmer Te in the dayside ionosphere of Mars. A description of the data used in this study is presented in Section 2. Results and discussion are presented in Sections 3 and 4 respectively. Conclusions are given in Section 5.

2. Data and overall analysis method

This study analyzed data recorded by the Mars Atmosphere and Volatile EvolutioN (MAVEN) mission [*Jakosky et al.*, 2015], which entered Mars orbit in late 2014. Data were analyzed between 2015-04-17 and 2015-05-15, when MAVEN's periapsis was closest to the sub-solar point to date, spanning a solar zenith angle (SZA) range of approximately 10°-40°. We assume that wave power from the Mars-solar wind interaction will propagate most efficiently into the Martian ionosphere at the sub-solar point based on observations at Venus. Landau damping of whistler mode waves from the Venetian ionosheath are known to be absorbed at the dayside ionosphere boundary, providing energy input into the dayside ionosphere. Such damping of waves is not an important energy source for the nightside Venetian ionosphere [*Taylor et al.*, 1979]. The relatively short range of sampled SZA reduces variability in the underlying neutral atmospheric density and temperature, which have been observed to vary with local time and can significantly affect the overlying ionosphere [*Andersson et al.*, 2017a]. Seasonal variability in solar EUV is assumed to be negligible over this relatively short time period. Data were analyzed below altitudes of 800 km and for a horizontal magnetic field only. A magnetic dip angle (defined as the angle between the local vertical and magnetic field) between 45° and 135° was defined as horizontal. This range was chosen based on the distribution of magnetic dip angles so that a suitable number of data points were available. The omission of vertical magnetic field conditions assumes that there is negligible plasma heating from electron precipitation under these conditions, such that plasma heating via wave-particle interactions is the primary heating mechanism for Te.

Electron densities and temperatures (Ne and Te), and 1D electric field wave spectra, were measured by the Langmuir Probe and Waves (LPW) instrument [*Andersson et al.*, 2014]. Both data sets were measured at a cadence of 4s below 500 km altitude, and 8s above. Ne and Te data exist at matching times and were derived from current-voltage (I-V) characteristics measured by the instrument; detailed discussion of the analysis method and the corresponding caveats can be found in *Ergun et al.* [2015] and *Andersson et al.* [2017b]. Just over 11,000 Te measurements were analyzed in this study. 1D electric field wave spectra between 2-100 Hz were analyzed from the LPW passive waves mode; the instrument cannot measure lower frequencies and the majority of wave power in the ionosphere lies below 100 Hz (Figure 1A). Wave power was normalized by multiplying by the width in frequency space (Hz) to produce units of $(\mathrm{V/m})^2$; the total wave power was calculated by summing all normalized wave power in the 2-100 Hz range. These spectra were 'paired' to the Ne and Te data in time so that each density and temperature measurement had a corresponding electric field wave power spectral measurement. The wave spectral measurements were obtained at the midpoint in time between the I-V data, i.e. 2s or 4s from the Te measurements and these differences are considered negligible for the purposes of this study. The 1D electric field wave spectra are calculated onboard the spacecraft via a Fast Fourier Transform (FFT) of high cadence time series 1D electric field data measured by the instrument. The instrument range limits density measurements from wave sounding to below $\sim$ 2x10^4 cm^{-3} as detailed in *Fowler et al.* [2017], and this is the upper density range for this study. At the sub-solar point, this corresponds to altitudes above about 200 km. For the remainder of this paper we refer to the total electric field wave power in the 2-100 Hz range simply as 'wave power'. The integrated electron density from the top of the ionosphere down to each Ne measurement point was calculated by integrating Ne from the measurement point up to 800 km altitude. This method assumed that the density profiles obtained by MAVEN are true vertical profiles, which is not a perfect assumption given the significant horizontal velocity ($\sim$ 4 kms^{-1}) of the spacecraft at periapsis.

3D magnetic field time series data were measured at a cadence of 32 Hz by the magnetometer (MAG) instrument, which is a fluxgate magnetometer [*Connerney et al.*, 2015]. A wavelet transform was performed on the ground on the magnitude of this time series data, to obtain the absolute magnetic field power spectra. Magnetic field power spectra were also paired to the LPW data and were required to lie within 5s of it. The 32 Hz cadence of MAG data meant that paired data typically lay within under a second of the LPW data and any errors associated with this pairing were considered negligible.

The total neutral atmospheric density (Nn) was calculated using data from the Neutral Gas and Ion Mass Spectrometer (NGIMS) instrument, which is a mass resolving ion spectrometer [*Mahaffy et al.*, 2015]. Individual neutral species densities are measured at cadences of around 2s; the total neutral density was obtained by summing the measured densities of the four dominant neutral species in the Martian atmosphere: N2, O, O2 and CO2. The total neutral density was also paired to the LPW data, and was required to lie within 5s. Changes within the neutral atmosphere typically occur over larger timescales and any errors associated with this pairing were assumed negligible. Due to ongoing calibration of outbound O densities, only inbound passes were used, reducing the number of data points to just over 8700 for a small subsection of the data analysis (Figure 2B) that involved Nn. The integrated total Nn was calculated in the same way as for integrated Ne.

The Solar Wind Electron Analyzer (SWEA) is a top-hat electrostatic analyzer that can resolve electron energy [*Mitchell et al.*, 2016]. The energy resolution of the instrument allows for the identification of 'photoelectron peaks' produced from the photoionization of atmospheric CO2 (e.g. *Frahm et al.* [2006]). The identification of such peaks was used to ensure that data from the ionosphere only, and not shocked solar wind plasma resulting from the Mars-solar wind interaction, were analyzed. The SWEA data used in this study were obtained at a cadence of 2s and were also paired to the LPW measurements.

The Solar Wind Ion Analyzer (SWIA) is an electrostatic top-hat ion analyzer that resolves energy but not ion mass [*Halekas et al.*, 2015a]. SWIA data were used to obtain estimates of the upstream solar wind dynamic pressure. Although MAVEN's orbit did not directly sample the solar wind for the data analyzed in this study, the upstream solar wind proton velocity and density can be inferred from the presence of so-called 'penetrating protons' observed by the instrument [*Halekas et al.*, 2015b, 2016]. Assuming the solar wind to be composed entirely of protons, the solar wind dynamic pressure was calculated for each MAVEN periapsis; these dynamic pressures were paired to the LPW data for each particular periapsis. This method assumed that the solar wind dynamic pressure was constant over the course of each periapsis pass, about 30 minutes.

Example time series plasma data for a single periapsis pass are shown in Figure 1. The electric and magnetic power spectra are in panels A and C respectively; panels B and D show these spectra spanning reduced frequency ranges of 2-100 Hz and 2-16 Hz respectively. The large electric field wave power observed across all frequencies between about 05:30 and 05:40 UTC occurs when Ne is greater than $\sim$ 2x10^{4} cm^{-3} and is a result of aliasing within the instrument, as discussed in *Fowler et al.* [2017]. Such time periods are not included in this analysis. The I-V derived Ne and Te are in panels E and F respectively. The total neutral density is in panel G; note the sharp jump just after 05:45 UTC in the profile. This is a result of background contamination from O and is why only inbound passes are used for analysis involving Nn. The SWEA electron energy spectrum is in panel H; photoelectron peaks from the photoionization of CO2 are observed at around 20 eV throughout most of the periapsis pass, showing where MAVEN is magnetically connected to the dayside ionosphere. Such photoelectrons are identified by an automated routine that analyzes the shape of the power spectrum at each timestep; panel I shows the output of this analysis; values below 2 were deemed representative of the ionosphere (this value was determined empirically). When MAVEN samples the very lowest altitudes between about 05:32 and 05:40 UTC, the photoelectron peak is no longer obvious due to frequent collisions with the neutral atmosphere. For this analysis, such times were still deemed representative of the ionosphere. The SWEA shape parameter was used primarily to exclude times where MAVEN sampled the shocked solar wind plasma, before about 05:17, and after about 05:46 UTC, in this example. The spacecraft altitude in the International Astronomical Union Mars planetocentric (IAU-Mars) reference frame is in panel J.

3. Results

The statistical median Te, as a function of wave power and integrated Ne (panel A), or integrated Nn (panel B), is shown in Figure 2. The integrated densities are a proxy for altitude and thus the y-axes have been inverted so that the largest integrated densities (lowest altitudes) lie at the bottom of the plots. Te does not reach such high values for panel B because the NGIMS instrument takes observations below 500 km and thus the largest Te values are not observed for these data. The figure contains varying pixel sizes such that each bin contains at least 15 data points, with most bins containing between 20 and 50 data points. For a given integrated Ne or Nn, Te increases as total wave power increases. For a given wave power, Te also increases as integrated density decreases. The maximum observed wave power decreases as integrated density increases. These broad trends are present for both panels. The sparser data coverage in panel B means that the remainder of this paper focusses on panel A.

By taking horizontal cuts across Figure 2A, the change in Te, for a specific integrated Ne, can be estimated as a function of wave power, and this is shown in Figure 3. Each line in the figure represents a horizontal cut through Figure 2A, where the color denotes the value of integrated Ne. The vertical axis in Figure 3 shows the change in Te, i.e., each line has been shifted so that the minimum value of Te is 0 K. Generally speaking, each line follows the same broad trend: Te increases linearly with the base 10 logarithm of wave power. The observed variability within each colored line mean that no single line stands out and thus, a straight line fit to all of the data is shown as the dashed line. The fit shows that, statistically, the rate of change of Te is independent of integrated Ne; the individual lines show that the maximum change in Te is however dependent upon integrated Ne. The fit is given by Equation 1:

$$\Delta Te = T0 + 447(log10[PF]) \tag{1}$$

Where $T0 = 5117$ K; $log10[PF]$ is the base 10 logarithm of the wave power, which is in units of (V/m)^2; and ΔTe has units of K. The important quantity to note from Equation 1 is the gradient, i.e. that Te increases by about 450 K for every order of magnitude increase in wave power.

The integrated electron density profiles analyzed in this study are shown as a function of altitude in Figure 4A and are meant as a rough guide to convert between integrated Ne and equivalent altitude. The highest observed values of integrated Ne ($\sim 10^6$ cm^{-2})

are observed close to and just below an altitude of 200 km; as the value of integrated Ne decreases, the spread of corresponding altitudes increases; integrated Ne of 10^4 cm^{-2} are observed between 300 km and 800 km altitude, for example.

The distribution of wave power with respect to integrated Ne is shown in Figure 4B, where line color represents a specific integrated Ne. The strongest wave powers are observed at the smallest integrated Ne (or highest altitudes); the strengths of observed wave powers decrease as integrated Ne (altitude) increases (decreases).

The distribution of solar wind dynamic pressures was used to create two sub-datasets: values of Te and wave power for low dynamic pressure conditions (the lower half of the dynamic pressure distribution), and values of Te and wave power for high dynamic pressure conditions (the upper half of the dynamic pressure distribution). The distributions of wave power for low and high dynamic pressures are shown in Figure 4C, by the solid blue and red lines respectively. The dashed blue and red lines show the number of measurements in the low and high condition bins respectively. Wave powers are slightly larger under higher solar wind dynamic pressures, but the change in overall distribution shape is small - changes of $\lesssim 5\%$ are observed in each of the bins.

4. Interpretation and discussion

Enhancements in Te of over 1000 K are observed to correlate with enhancements in wave power (Figures 2 and 3). The local electron gyrofrequency in the Martian ionosphere (where the magnitude of the magnetic field is typically a few tens of nT) is a few thousand Hz; thus, the observed wave powers in the 2-100 Hz range appear to provide low frequency heating of the ionospheric electrons. Similar, low frequency electron heating has been observed in the terrestrial inner magnetosphere (e.g. *Chaston et al.* [2015]) and the terrestrial E region (e.g. *Schlegel and St-Maurice* [1981]; *St-Maurice et al.* [1981]; *St-Maurice and Laher* [1985]). Similar enhancements in Te of ~ 1000 K have been observed in the terrestrial E region (e.g. *St-Maurice et al.* [1981]), although we note that the terrestrial E region is much more collisional in nature than the ionospheric region investigated in this study (namely, at and above the Martian exobase). The lack of magnetic field wave power in Figure 1D suggests that waves above about 2 Hz in the Martian ionosphere are electrostatic in nature. Significant magnetic wave power is observed below 2 Hz (Figure 1B) but is not the focus of this study.

The largest observed values of wave power decrease as integrated Ne increases (Figure 2), suggesting that the ionospheric plasma is absorbing this wave energy as it (is assumed to) propagates downward in the ionosphere. The distribution of wave power as a function of integrated Ne (Figure 4B) further supports this interpretation; the largest wave powers are observed predominately at the lowest integrated Ne, and the smallest wave powers are observed primarily at the largest integrated Ne. These correlations were most obvious when binning data by integrated Ne and Nn, rather than altitude, further supporting these interpretations. Integrated Ne should be somewhat dependent on integrated Nn and the similarities between Figure 2A and B are not surprising. The observed wave powers may also heat ions, although the frequency range analyzed in this study lies well above (by a factor of at least several tens) the local ion gyrofrequencies. Ion temperatures are currently unavailable from the MAVEN mission due to ongoing calibration efforts and are not the focus of this study.

The MAVEN observations show that very little wave power exists below an integrated Ne of about 10^6 cm^{-3}, or about 200 km altitude (Figure 4B). Larger wave powers exist when the solar wind dynamic pressure is stronger (Figure 4C), although the changes in distribution shapes are small. Given Figures 2 and 3, conditions of stronger upstream solar wind dynamic pressure will result in warmer Te.

It is assumed that the observed increases in Te are due primarily to electron heating via wave-particle interactions with the observed wave powers. Other sources of plasma heating are likely present in the Martian ionosphere and may contribute to the observed increases in Te; the analysis method minimizes these additional heating contributions. Solar EUV heating enhances the neutral atmospheric temperature, which in turn increases Te through collisions below the exobase. The relatively short time range that this study covers means that seasonal solar EUV effects are negligible. Short term variations in EUV intensity of 10%-20% are present due to solar rotation. This study analyzed data at and above the exobase and thus collisions are rare and solar heating dominates only at much lower altitudes, in the collision dominated regime (e.g. *Fox and Dalgarno* [1979]). We thus deem solar EUV effects negligible. The analysis of only horizontal magnetic field cases limits the effects of electron precipitation, which can be a source of significant atmospheric heating and ionization (e.g. *Verigin et al.* [1991]; *Haider et al.* [1992]; *Fox* [1993b]; *Lillis et al.* [2009, 2011]; *Lillis and Fang* [2015]; *Fowler et al.* [2015]).

5. Conclusions

The instrument suite carried by the MAVEN spacecraft allows for the first time at Mars in-situ measurements of electric field wave power to be made within the Martian ionosphere, that can be compared with measurements of the electron temperature, Te. This study analyzed one month of MAVEN data where periapsis was close to the sub-solar point, to identify correlations between observed Te and electric field wave power in the 2-100 Hz range. The effects of additional heating sources, such as seasonal variations in solar EUV intensity, heat inflow and precipitating electrons, have been minimized by analyzing data from a relatively short period of time and under horizontal magnetic field conditions. The analysis shows that electron heating via the observed wave powers can account for a substantial (but likely not complete) fraction of the observed discrepancies between measured and previously modeled Te: enhancements in Te of over 1000 K were observed for the strongest wave powers. Previously modeled Te can be 2000 K or more colder than measured values (e.g. *Choi et al.* [1998]; *Matta et al.* [2014]; *Sakai et al.* [2016]) and thus, additional heating sources (such as solar EUV and precipitating electrons) are still likely present in the ionosphere.

Total wave power within the 2-100 Hz frequency range were observed to span values between approximately 10^{-12} to 10^{-9} $(\mathrm{V/m})^2$ in the Martian ionosphere. These wave powers showed a strong dependence on integrated electron density, suggesting that energy is absorbed by the ionosphere as these waves (are assumed to) propagate downward.

Slightly larger wave powers were observed under stronger solar wind upstream dynamic pressures; a more extreme solar wind in the past could have resulted in warmer Te and enhanced ion escape.

Wave power at frequencies close to the typical ion cyclotron frequencies ($\sim 10^{-2}$ Hz) are likely to heat ionospheric ions, although the electric field instrument on MAVEN does not sample below 2 Hz. Ion temperatures are also not yet available from the MAVEN data due to ongoing calibration, but would be a worthwhile channel of investigation in the future.

Determination of the exact nature and source of the observed waves was outside the scope of this study. Obliquely propagating whistler mode waves produced by the Venus-solar wind interaction have been observed to heat the Venetian ionosphere [*Taylor et al.*, 1979; *Scarf et al.*, 1980]. Given the unmagnetized nature of Mars and Venus, such a mechanism may also be active at Mars, although the apparent electrostatic nature of the waves observed in this study means that their source remains unknown.

Acknowledgments. We gratefully acknowledge the valuable discussions and input from Roger Yelle. We also thank the anonymous reviewers for their valuable feedback on the manuscript.

Work at LASP and SSL was supported by NASA funding for the MAVEN project through the Mars Exploration Program. Data used in this study is available on the NASA Planetary Data System, via http://ppi.pds.nasa.gov/project/maven/.html.

This work was partially supported by the CNES for the part based on observations with the SWEA instrument embarked on Maven.

References

Andersson, L., R. Ergun, and A. Stewart (2010), The combined atmospheric photochemistry and ion tracing code: Reproducing the Viking lander results and initial outflow results, *Icarus*, *206*(1), 120–129.

Andersson, L., R. E. Ergun, G. T. Delory, A. Eriksson, J. Westfall, H. Reed, J. McCauly, D. Summers, and D. Meyers (2014), The Langmuir Probe and Waves (LPW) instrument for MAVEN, *Space Science Reviews*, pp. 1–26.

Andersson, L., C. Fowler, A. Nagy, R. Yelle, T. Cravens, S. Bougher, A. Burns, W. Peterson, B. Jakosky, M. Benna, R. Ergun, A. Woodson, and J. Connerney (2017a), Diurnal variations in electron temperature in the Mars ionosphere, *Geophysical Research Letters*, *Under review*.

Andersson, L., T. Chamandy, C. Fowler, R. Ergun, A. Eriksson, G. Delory, D. Andrews, A. Woodson, J. Connerney, and B. Jakosky (2017b), Electron and Density Profiles of the Martian Ionosphere: A Statistical Analysis, *Journal of Geophysical Research: Space Physics*, *Under review*.

Brain, D., F. Bagenal, M. Acuna, J. Connerney, D. Crider, C. Mazelle, D. Mitchell, and N. Ness (2002), Observations of low-frequency electromagnetic plasma waves upstream from the Martian shock, *Journal of Geophysical Research: Space Physics*, *107*(A6).

Chaston, C., J. Bonnell, J. Wygant, C. Kletzing, G. Reeves, A. Gerrard, L. Lanzerotti, and C. Smith (2015), Extreme ionospheric ion energization and electron heating in Alfvén waves in the storm time inner magnetosphere, *Geophysical Research Letters*.

Chen, R., T. Cravens, and A. Nagy (1978), The Martian ionosphere in light of the Viking observations, *Journal of Geophysical Research: Space Physics*, *83*(A8), 3871–3876.

Choi, Y., J. Kim, K. Min, A. Nagy, and K. Oyama (1998), Effect of the magnetic field on the energetics of Mars ionosphere, *Geophysical Research Letters*, *25*(14), 2753–2756.

Collinson, G., D. Mitchell, A. Glocer, J. Grebowsky, W. Peterson, J. Connerney, L. Andersson, J. Espley, C. Mazelle, J.-A. Sauvaud, et al. (2015), Electric Mars: The first direct measurement of an upper limit for the Martian polar wind electric potential, *Geophysical Research Letters*, *42*(21), 9128–9134.

Connerney, J. E. P., J. Espley, P. Lawton, S. Murphy, J. Odom, R. Oliversen, and D. Sheppard (2015), The MAVEN Magnetic Field Investigation, *Space Science Reviews*, doi: 10.1007/s11214-015-0169-4.

Cravens, T., T. Gombosi, J. Kozyra, A. Nagy, L. Brace, and W. Knudsen (1980), Model calculations of the dayside ionosphere of Venus - Energetics, *Journal of Geophysical Research*, *85*, 7778–7786.

Cui, J., M. Galand, S. Zhang, E. Vigren, and H. Zou (2015), The electron thermal structure in the dayside Martian ionosphere implied by the MGS radio occultation data, *Journal of Geophysical Research: Planets*, *120*(2), 278–286.

DiBraccio, G. A., J. Espley, J. R. Gruesbeck, J. E. Connerney, D. A. Brain, J. S. Halekas, D. L. Mitchell, J. P. McFadden, Y. Harada, R. Livi, et al. (2015), Magnetotail dynamics at Mars: Initial MAVEN observations, *Geophysical Research Letters*, *42*(21), 8828–8837.

Ergun, R., L. Andersson, W. Peterson, D. Brain, G. Delory, D. Mitchell, R. Lin, and A. Yau (2006), Role of plasma waves in Mars' atmospheric loss, *Geophysical research* *letters*, *33*(14).

Ergun, R., M. Morooka, L. Andersson, C. Fowler, G. Delory, D. J. Andrews, A. I. Eriksson, T. McEnulty, and B. Jakosky (2015), Dayside electron temperature and density profiles at Mars: First results from the MAVEN Langmuir probe and waves instrument, *Geophysical Research Letters*, *42*(21), 8846–8853.

Ergun, R., L. Andersson, C. Fowler, A. Woodson, T. Weber, G. Delory, D. J. Andrews, A. I. Eriksson, T. McEnulty, M. Morooka, et al. (2016), Enhanced O2+ loss at Mars due to an ambipolar electric field from electron heating, *Journal of Geophysical Research: Space Physics*, *121*(5), 4668–4678.

Espley, J., P. Cloutier, D. Brain, D. Crider, and M. Acuña (2004), Observations of low-frequency magnetic oscillations in the Martian magnetosheath, magnetic pileup region, and tail, *Journal of Geophysical Research: Space Physics*, *109*(A7).

Fowler, C., L. Andersson, R. Ergun, M. Morooka, G. Delory, D. J. Andrews, R. J. Lillis, T. McEnulty, T. Weber, T. Chamandy, et al. (2015), The first in situ electron temperature and density measurements of the Martian nightside ionosphere, *Geophysical Research Letters*, *42*(21), 8854–8861.

Fowler, C., L. Andersson, J. Halekas, J. Espley, C. Mazelle, E. Coughlin, R. Ergun, D. Andrews, J. Connerney, and B. Jakosky (2017), Electric and magnetic variations in the near Mars environment, *Journal of Geophysical Research: Space Physics*, *Under Review*.

Fox, J. L. (1993a), On the escape of oxygen and hydrogen from Mars, *Geophysical research letters*, *20*(17), 1747–1750.

Fox, J. L. (1993b), Upper limits to the nightside ionosphere of Mars, *Geophysical Research Letters*, *20*(13), 1339.

Fox, J. L., and A. Dalgarno (1979), Ionization, luminosity, and heating of the upper atmosphere of Mars, *Journal of Geophysical Research: Space Physics*, *84*(A12), 7315–7333.

Fox, J. L., and A. B. Hać (2009), Photochemical escape of oxygen from Mars: A comparison of the exobase approximation to a Monte Carlo method, *Icarus*, *204*(2), 527–544.

Frahm, R., J. Winningham, J. Sharber, J. Scherrer, S. Jeffers, A. Coates, D. Linder, D. Kataria, R. Lundin, S. Barabash, et al. (2006), Carbon dioxide photoelectron energy peaks at Mars, *Icarus*, *182*(2), 371–382.

Haider, S., J. Kim, A. Nagy, C. Keller, M. Verigin, K. Gringauz, N. Shutte, K. Szego, and P. Kiraly (1992), Calculated ionization rates, ion densities, and airglow emission rates due to precipitating electrons in the nightside ionosphere of Mars, *Journal of Geophysical Research: Space Physics (1978–2012)*, *97*(A7), 10,637–10,641.

Halekas, J., E. Taylor, G. Dalton, G. Johnson, D. Curtis, J. McFadden, D. Mitchell, R. Lin, and B. Jakosky (2015a), The Solar Wind Ion Analyzer for MAVEN, *Space Science Reviews*, doi:10.1007/s11214-013-0029-z.

Halekas, J., R. Lillis, D. Mitchell, T. Cravens, C. Mazelle, J. Connerney, J. Espley, P. Mahaffy, M. Benna, B. Jakosky, et al. (2015b), MAVEN observations of solar wind hydrogen deposition in the atmosphere of Mars, *Geophysical Research Letters*, *42*(21), 8901–8909.

Halekas, J., S. Ruhunusiri, Y. Harada, G. Collinson, D. Mitchell, C. Mazelle, J. McFadden, J. Connerney, J. Espley, F. Eparvier, et al. (2016), Structure, dynamics, and seasonal variability of the mars-solar wind interaction: MAVEN solar wind ion analyzer inflight performance and science results, *Journal of Geophysical Research: Space Physics*.

Hanson, W., and G. Mantas (1988), Viking electron temperature measurements: Evidence for a magnetic field in the Martian ionosphere, *Journal of Geophysical Research: Space Physics*, *93*(A7), 7538–7544.

Jakosky, B. M., R. P. Lin, J. M. Grebowsky, J. G. Luhmann, D. F. Mitchell, G. Beutelschies, T. Priser, M. Acuna, L. Andersson, D. Baird, et al. (2015), The Mars Atmosphere and Volatile Evolution (MAVEN) Mission, *Space Science Reviews*, pp. 1–46.

Lee, Y., M. R. Combi, V. Tenishev, S. W. Bougher, and R. J. Lillis (2015), Hot oxygen corona at Mars and the photochemical escape of oxygen: Improved description of the thermosphere, ionosphere, and exosphere, *Journal of Geophysical Research: Planets*, *120*(11), 1880–1892.

Lillis, R. J., and X. Fang (2015), Electron impact ionization in the Martian atmosphere: interplay between scattering and crustal magnetic field effects, *Journal of Geophysical Research*.

Lillis, R. J., M. O. Fillingim, L. M. Peticolas, D. A. Brain, R. P. Lin, and S. W. Bougher (2009), Nightside ionosphere of Mars: Modeling the effects of crustal magnetic fields and electron pitch angle distributions on electron impact ionization, *Journal of Geophysical Research: Planets (1991–2012)*, *114*(E11).

Lillis, R. J., M. O. Fillingim, and D. A. Brain (2011), Three-dimensional structure of the Martian nightside ionosphere: Predicted rates of impact ionization from Mars Global Surveyor magnetometer and electron reflectometer measurements of precipitating electrons, *Journal of Geophysical Research: Space Physics (1978–2012)*, *116*(A12).

Lillis, R. J., D. A. Brain, S. W. Bougher, F. Leblanc, J. G. Luhmann, B. M. Jakosky, R. Modolo, J. Fox, J. Deighan, X. Fang, et al. (2015), Characterizing atmospheric escape from Mars today and through time, with MAVEN, *Space Science Reviews*, *195*(1-4), 357–422.

Mahaffy, P. R., M. Benna, T. King, D. N. Harpold, R. Arvey, M. Barciniak, M. Bendt, D. Carrigan, T. Errigo, V. Holmes, et al. (2015), The neutral gas and ion mass spectrometer on the Mars atmosphere and volatile evolution mission, *Space Science Reviews*, *195*(1-4), 49–73.

Matta, M., M. Galand, L. Moore, M. Mendillo, and P. Withers (2014), Numerical simulations of ion and electron temperatures in the ionosphere of Mars: Multiple ions and diurnal variations, *Icarus*, *227*, 78–88.

Mitchell, D. L., C. Mazelle, J.-A. Sauvaud, J.-J. Thocaven, J. Rouzaud, A. Fedorov, P. Rouger, D. Toublanc, E. Taylor, D. Gordon, M. Robinson, S. Heavner, P. Turin, M. Diaz-Aguado, D. W. Curtis, R. P. Lin, and B. M. Jakosky (2016), The MAVEN Solar Wind Electron Analyzer, *Space Science Reviews*, *200*(1), 495–528, doi:10.1007/s11214-015-0232-1.

Moses, S., F. Coroniti, and F. Scarf (1988), Expectations for the microphysics of the Mars-solar wind interaction, *Geophysical Research Letters*, *15*(5), 429–432.

Sakai, S., L. Andersson, T. E. Cravens, D. L. Mitchell, C. Mazelle, A. Rahmati, C. M. Fowler, S. W. Bougher, E. Thiemann, F. G. Eparvier, et al. (2016), Electron energetics in the Martian dayside ionosphere: Model comparisons with MAVEN data, *Journal of*

Geophysical Research: Space Physics, *121*(7), 7049–7066.

Scarf, F., W. Taylor, C. Russell, and R. Elphic (1980), Pioneer Venus plasma wave observations: The solar wind-Venus interaction, *Journal of Geophysical Research: Space Physics*, *85*(A13), 7599–7612.

Schlegel, K., and J. St-Maurice (1981), Anomalous heating of the polar E region by unstable plasma waves 1. Observations, *Journal of Geophysical Research: Space Physics*, *86*(A3), 1447–1452.

Schunk, R., and A. Nagy (2009), *Ionospheres: physics, plasma physics, and chemistry*, Cambridge university press.

Shapiro, V., K. Szegö, S. Ride, A. Nagy, and V. Shevchenko (1995), On the interaction between the shocked solar wind and the planetary ions on the dayside of Venus, *Journal of Geophysical Research: Space Physics*, *100*(A11), 21,289–21,305.

St-Maurice, J., K. Schlegel, and P. Banks (1981), Anomalous Heating of the Polar E Region 2. Theory, *Journal of Geophysical Research*, *86*(A3), 1453–1462.

St-Maurice, J.-P., and R. Laher (1985), Are observed broadband plasma wave amplitudes large enough to explain the enhanced electron temperatures of the high-latitude E region?, *Journal of Geophysical Research: Space Physics*, *90*(A3), 2843–2850.

Taylor, W., F. Scarf, C. Russell, and L. Brace (1979), Absorption of whistler mode waves in the ionosphere of Venus, *Science*, *205*(4401), 112–114.

Verigin, M., K. Gringauz, N. Shutte, S. Haider, K. Szego, P. Kiraly, A. Nagy, and T. Gombosi (1991), On the possible source of the ionization in the nighttime Martian ionosphere: 1. Phobos 2. HARP electron spectrometer measurements, *Journal of*

Geophysical Research: Space Physics (1978–2012), *96*(A11), 19,307–19,313.

FIG1_PFP_fig2.pdf

Figure 1. Example time series plasma data for a single periapsis pass. The panels show: A and C: electric and magnetic power spectra, respectively; B and D: electric and magnetic power spectra between 2-100 Hz and 2-16 Hz, respectively; E and F: Ne and Te derived from the LPW I-V characteristics; G: total neutral density from NGIMS; H and I: SWEA energy spectra, and photoelectron shape parameter, respectively; J: spacecraft altitude. Panels A and B have units of $V^2m^{-2}Hz^{-1}$; panels C and D: T^2Hz^{-1}; panel H: eV (eV cm^2 s sr)$^{-1}$.

FIG2_Te_EP_Ne_Nn_Bhor.pdf

Figure 2. Statistical median electron temperature Te, as a function of total electric field wave power and integrated electron density (panel A), and as a function of total electric field wave power and integrated total neutral density (panel B).

FIG3_Del_Te_EP_neint2_Bhor.pdf

Figure 3. Horizontal cuts through Figure 2A, showing Te as a function of total electric field wave power, for specific integrated electron densities. Te have been shifted such that the vertical axis shows the change in Te, from the coldest value measured for each line. The dashed black line is a fit to all data points. Note that Figure 4A can be used to obtain an approximate conversion between integrated electron density and altitude.

FIG4_EP_dists.pdf

Figure 4. A: The integrated electron density profiles analyzed in this study, as a function of altitude. B: Distributions of total electric field wave power for various values of integrated electron density. C: The blue and red solid lines show the distributions of total electric field wave power for low and high solar wind dynamic pressures, respectively (left hand vertical axis). The dashed lines show the number of data points in each bin (right hand vertical axis).

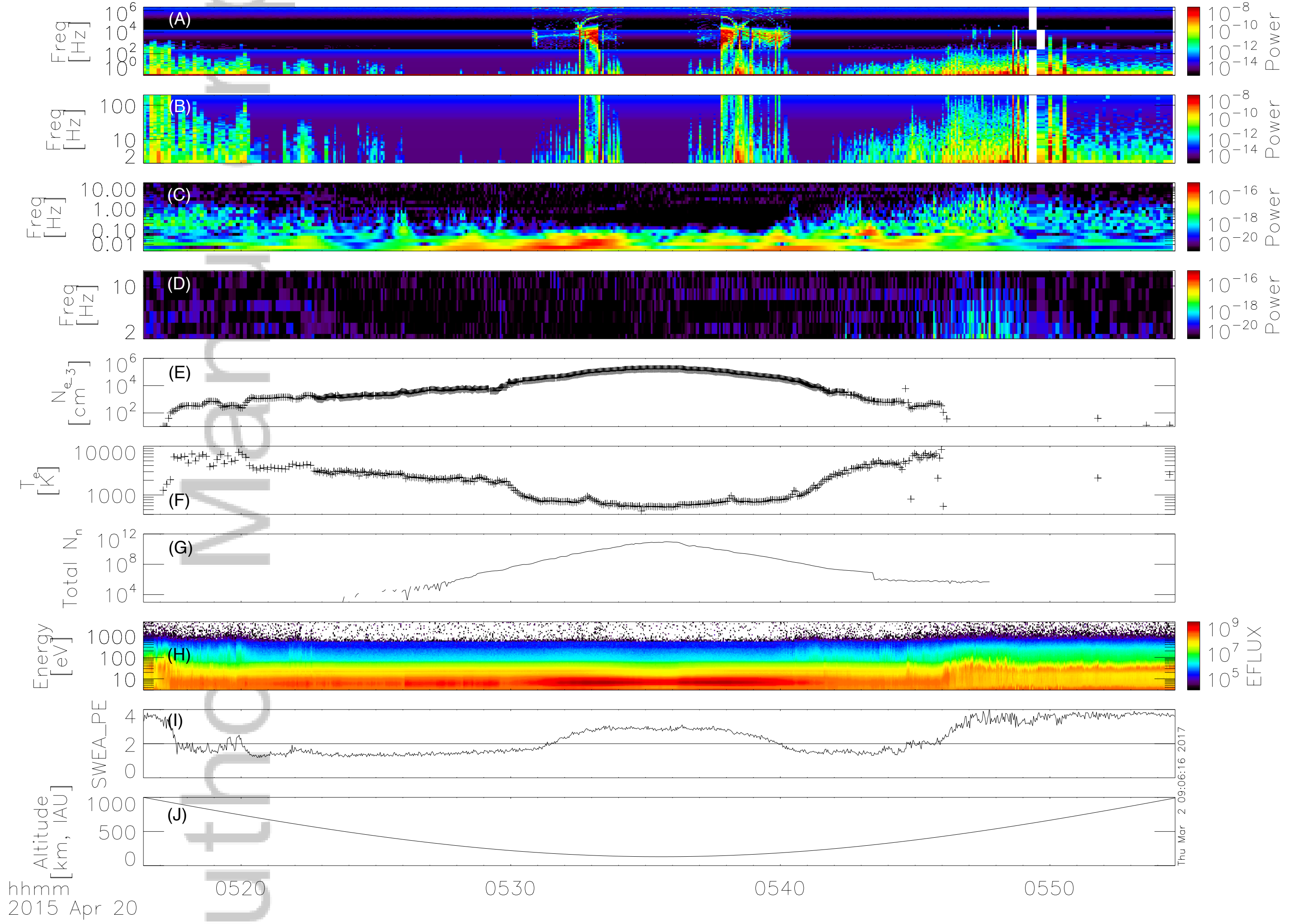
(A)
Freq [Hz]
Power
(B)
Freq [Hz]
Power
(C)
Freq [Hz]
Power
(D)
Freq [Hz]
Power
(E)
N_e [cm^-3]
(F)
T_e [K]
(G)
Total N_n
(H)
Energy [eV]
EFLUX
(I)
SWEA_PE
(J)
Altitude [km, IAU]
Thu Mar 2 09:06:16 2017
hhmm
2015 Apr 20
0520
0530
0540
0550

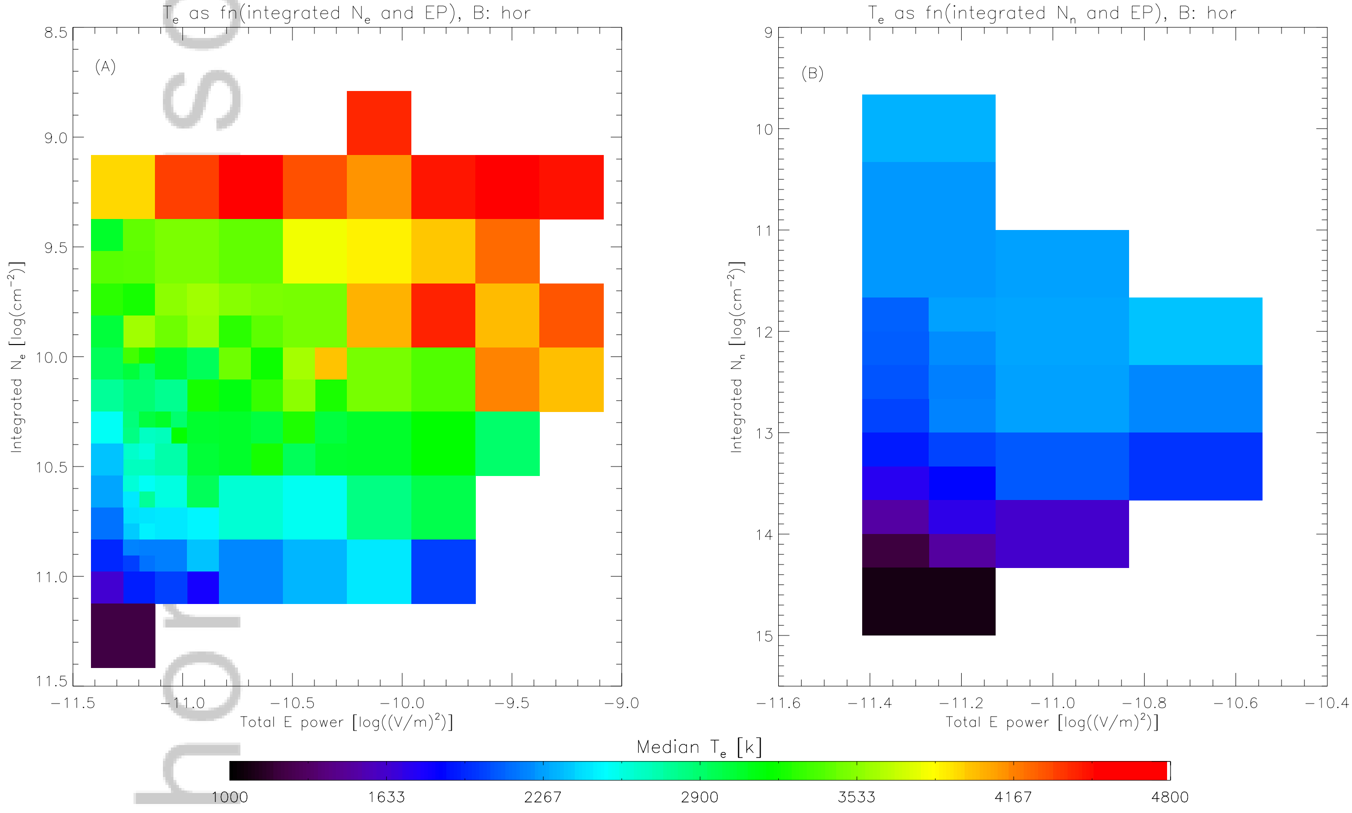

Te as fn(integrated Ne and EP), B: hor
(A)
Integrated Ne [log(cm−2)]
8.5
9.0
9.5
10.0
10.5
11.0
11.5
−11.5
−11.0
−10.5
−10.0
−9.5
−9.0
Total E power [log((V/m)2)]
Te as fn(integrated Nn and EP), B: hor
(B)
Integrated Nn [log(cm−2)]
9
10
11
12
13
14
15
−11.6
−11.4
−11.2
−11.0
−10.8
−10.6
−10.4
Total E power [log((V/m)2)]
Median Te [k]
1000
1633
2267
2900
3533
4167
4800

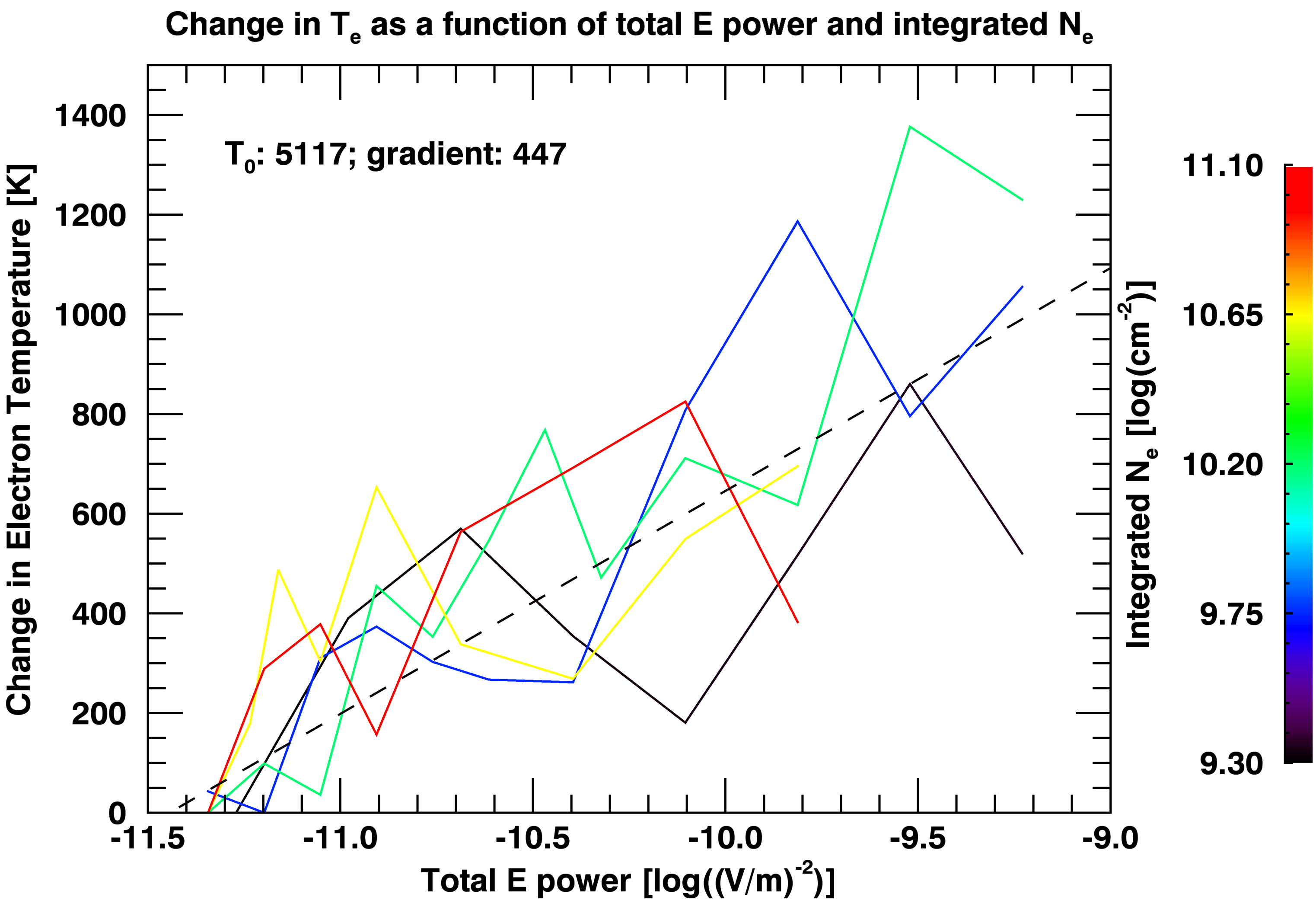

Change in T_e as a function of total E power and integrated N_e
T_0: 5117; gradient: 447
Change in Electron Temperature [K]
0
200
400
600
800
1000
1200
1400
-11.5
-11.0
-10.5
-10.0
-9.5
-9.0
Total E power [log((V/m)$^{-2}$)]
Integrated N_e [log(cm^{-2})]
11.10
10.65
10.20
9.75
9.30

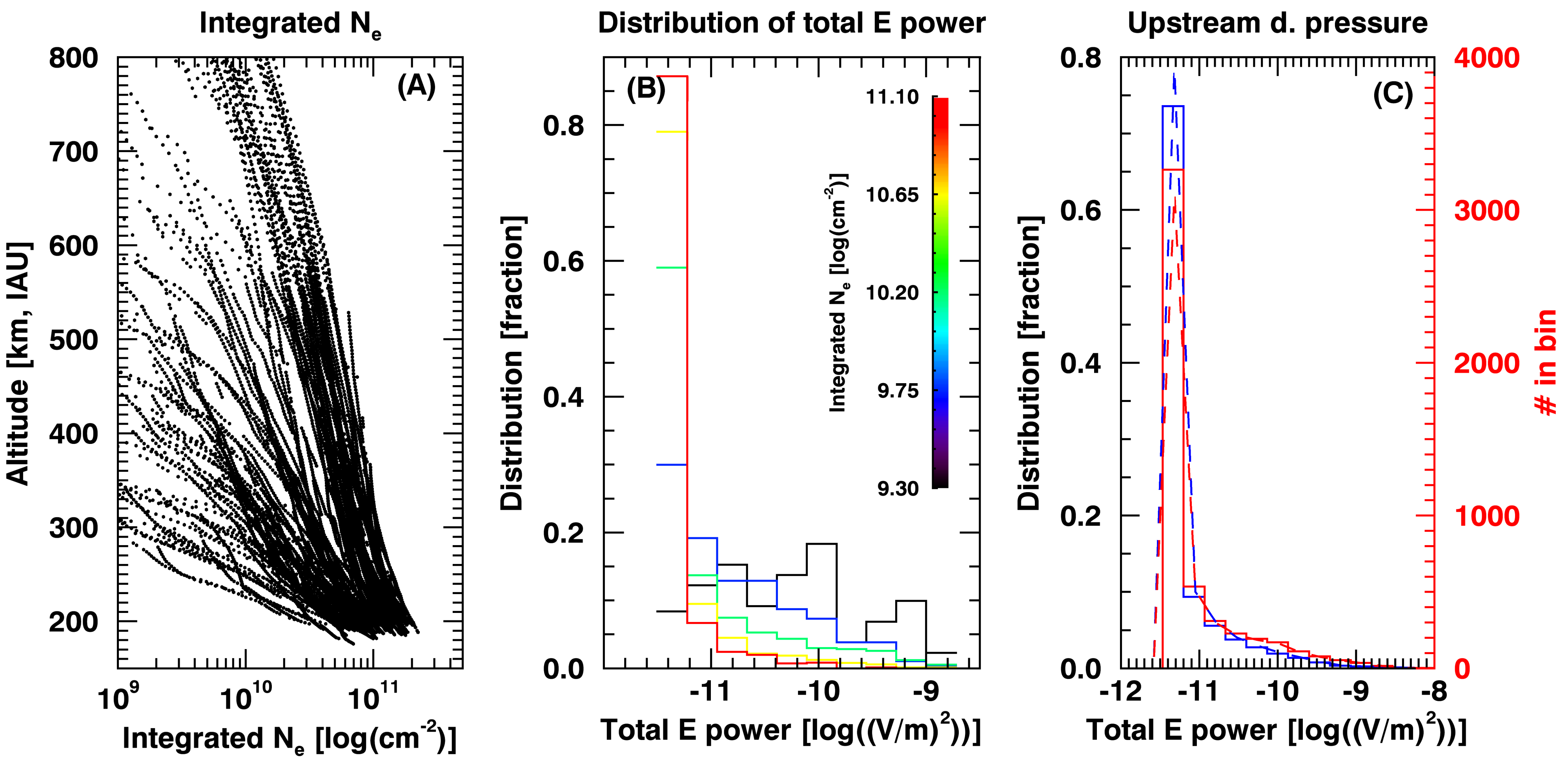

Integrated N_e
(A)
Altitude [km, IAU]
800
700
600
500
400
300
200
10^9
10^{10}
10^{11}
Integrated N_e [log(cm^{-2})]
Distribution of total E power
(B)
Distribution [fraction]
0.8
0.6
0.4
0.2
0.0
-11
-10
-9
Total E power [log((V/m)^2))]
Integrated N_e [log(cm^{-2})]
11.10
10.65
10.20
9.75
9.30
Upstream d. pressure
(C)
Distribution [fraction]
0.8
0.6
0.4
0.2
0.0
-12
-11
-10
-9
-8
Total E power [log((V/m)^2))]
4000
3000
2000
1000
0
in bin